Drone With Integrated Moving Baseline System and Time-Domain Autofocus Algorithm for High-Resolution SAR Images

Peter Brotzer, *Member, IEEE*, Daniel Henke, David Small, *Senior Member, IEEE*, Emiliano Casalini, Sébastien Guillaume, Rolf Vogt, and Elías Méndez Domínguez, *Member, IEEE*

***Abstract*—The demand for drone-based synthetic aperture radar (SAR) systems is growing, especially for applications in cases where satellites or airborne systems are not sufficiently flexible. However, the combination of a long operating range and high spatial resolution causes the atmosphere to pose challenges for these systems. In this article, we present our K-band drone system that has a long range sensibility through modification to a commercially available radar. In addition, a moving baseline configuration has been integrated to ensure accurate attitude data, especially the heading. The desired spatial resolution is achieved by our proposed autofocus algorithm based on image sharpness. It is designed to also work in challenging cases of nonlinear flight paths and can be integrated into a processing framework based on back-projection. Several experiments were conducted to demonstrate the drone system's capabilities. These included a comparison with an established airborne radar: MIRANDA35. The obtained results demonstrate the ability of the drone SAR system to map wide areas at high spatial resolution.**

***Index Terms*—Autofocus, drone, frequency-modulated continuous wave (FMCW), K-band, synthetic aperture radar (SAR), uncrewed aerial vehicle.**

I. Introduction

DRONE-BASED synthetic aperture radar (SAR) drone systems open up possibilities where airborne systems and satellite systems are less suitable. The flexible flight paths of drones allow the optimization of data acquisition patterns over areas of interest. Multiaspect imaging of objects, time series with high repetition rates, and independence from third parties begin the list of notable benefits. In addition, their comparatively low flight altitude makes it relatively straightforward to use high-frequency radars. Due to the commercial availability of small, frequency-modulated continuous-wave (FMCW) radars, SAR systems can be cost-effectively integrated on drones. Nevertheless, certain tradeoffs between sensor quality and drone payload are necessary. The required high-precision inertial measurement units (IMUs) for high-resolution SAR systems are often too heavy or costly to integrate into commercial off-the-shelf drone systems. Software-based solutions for focusing are, therefore, widely used, though their applicability can depend on the characteristics of a specific scene [1]. Another limitation may arise due to the transmission power of the radar. Enhanced power supplies would be required for mapping distant objects with a sufficient signal-to-noise ratio.

Although drone-based SAR is still a relatively new research area, several research groups have proposed hardware setups and experimentally demonstrated various applications. For example, it has been shown that ground-penetrating SAR drones can be used to detect land mines [2], [3], [4]. Another wide range of applications falls in the category of differential SAR interferometry [5], [6], [7]. With a triband SAR system (C-, L-, and P-bands) on their drone, Oré et al. [8] were able to predict the harvest date and the productivity of sugarcane. They can cover wide ranges; however, they used lower frequencies specifically to fit their application to natural targets. A low-cost high-resolution FMCW SAR drone operating at 77-GHz central frequency with a 1-GHz range bandwidth that did not use a dedicated inertial navigation system (INS) or a global positioning system (GPS) was presented by Bekar et al. [9]. They achieved a cross-range resolution of 2 cm at short ranges. While this is an impressive result, often it is preferable to cover a wider area. A robust autofocus method without using GPS data for their Ka-band, 2-GHz bandwidth octocopter, was presented by Liu et al. [10]. Results were shown using data acquired at flight altitudes up to 120 m with an antenna depression angle of 45°. While they were able to cover a wide area, the lack of an autofocus method leads to a resolution that could be improved. A demonstration of simultaneous localization and imaging with their FUSAR-Ku drone was provided by Luomei et al. [11]. An azimuth resolution of 10 cm was achieved with simultaneous centimeter-to-decimeter 3-D self-positioning accuracy. A restricting factor could be its usage of 7×7 grid point targets with a spacing of 25 m to derive the position errors. This approach works well at the altitude of 450 m but might be a problem for drones flying at lower altitudes. With their small C-band uncrewed-aerial-vehicle-based SAR system,

Manuscript received 18 August 2023; revised 16 October 2023 and 11 December 2023; accepted 14 December 2023. Date of publication 25 December 2023; date of current version 4 January 2024. This work was supported in part by armasuisse W+T. *(Corresponding author: Peter Brotzer.)*

Peter Brotzer, Daniel Henke, David Small, Emiliano Casalini, and Elías Méndez Domínguez are with Remote Sensing Laboratories, Department of Geography, University of Zurich, CH-8057 Zurich, Switzerland (e-mail: peter.brotzer@geo.uzh.ch; daniel.henke@geo.uzh.ch; david.small@geo.uzh.ch; emiliano.casalini@geo.uzh.ch; elias.mendez@geo.uzh.ch).

Sébastien Guillaume is with the Département d'Environnement Construit and Géoinformation, Institute of Territorial Engineering, HEIG-VD, CH-1401 Yverdon-les-Bains, Switzerland (e-mail: sebastien.guillaume@heig-vd.ch).

Rolf Vogt is with Wireless Telecommunication, Engineering and Computer Science, Bern University of Applied Sciences, CH-2502 Biel, Switzerland (e-mail: rolf.vogt@bfh.ch).

Digital Object Identifier 10.1109/JSTARS.2023.3345954

Svedin et al. [12] investigated, among other things, the influence of attitude data on image quality. However, their low-cost IMU was not able to provide accurate enough attitude data for the zigzag trajectory of the drone.

In this article, we introduce a K-band SAR drone with several state-of-the-art hardware extensions and demonstrate how to focus high-quality SAR images using an advanced autofocus algorithm. On the hardware side, we rely on a modified FMCW Radarbook2 sensor [13] operating at 24 GHz with a bandwidth of 700 MHz. We improved the system by installing a power amplifier so that the adjustable transmit power can reach up to 30.5 dBm. This allows one to map objects at a distance of up to 400 m. Another innovative concept of the hardware setup is a moving baseline navigation system consisting of four differential global navigation satellite system (DGNSS) receivers and an INS. It serves as a reliable, lightweight, and cost-effective alternative to a high-end IMU. Such a setup could be beneficial for lightweight systems like in [12]. On the software side, we suggest a combination of an optimal-path-based solution [14], [15] and a modified version of Ash's autofocus [16] to further improve image quality. A big advantage of this focusing algorithm is that it can be integrated in a time-domain back-projection (TDBP) processing scheme, producing images in map geometry. Already by design, nonlinear flight paths can be handled easier with TDBP [17]. A contrast-based method was chosen, as it serves as a reliable estimator independent of size of the positioning error and the flight altitude. Phase-based methods tend to work only for small errors. By applying the optimal path solution, we compensate for larger errors that could not otherwise be dealt with by Ash's method alone. We demonstrate the accuracy of our system and the developed autofocus algorithm in several experiments, including a comparison with MIRANDA35 airborne data [18]. The azimuth and range resolutions reach values up to 2.3 and 19 cm, respectively, which are close to the system's theoretical values.

The rest of this article is organized as follows. In Section II, the hardware setup of the SAR drone is described, and the experimental setups are presented. This is followed by the methods in Section III. Each of the experiments is described in Section IV, followed by its results. Discussion of the results is given in Section V. Finally, Section VI concludes this article.

II. Hardware

The drone has several components for different tasks. We first describe the radar and its characteristics, followed by the drone's navigation system and the optical camera.

A. Radar

The modified FMCW K-band Radarbook2 radar is mounted on a DJI Matrice 600 Pro drone, as shown in Fig. 1. It operates at 24 GHz with a range bandwidth of 700 MHz. Additional properties are summarized in Table I. The standard version of the Radarbook2 features two patch antenna arrays with a transmission power of 18 dBm. To increase the signal strength up to 30.5 dBm, a front-end amplifier was connected to an external power amplifier. The gain can be varied stepwise, between being switched OFF up to the mentioned maximum. As the amplifier has a power consumption of 7 W, the heat generated is dissipated with a small lightweight heat sink. As a new transmitting antenna, a horn antenna is used. The reason for this is that the voltage standing wave ratio of patch antennas is not small enough for the amplifier. With an amplifier power of 30.5 dBm and an antenna gain of 20.3 dB, an equivalent isotropically radiated power (EIRP) of up to 50.8 dBm can be achieved. The 3-dB antenna beamwidth in azimuth is 14°, while the elevation beamwidth is 16°.

Fig. 1. K-band SAR drone platform with the moving baseline system and the optical camera.

TABLE I
System Parameters of SAR Platforms

Parameter	Radarbook2	MIRANDA35
Carrier frequency	24 GHz	35 GHz
Bandwidth	700 MHz	1500 MHz
Pulse repetition frequency	1 kHz	1.5 kHz
Range resolution	19 cm	13 cm
Azimuth resolution	2.3 cm	6.8 cm
Transmission power	up to 30.5 dBm	up to 40 dBm
Near range	$\sim$ 0 m	1700 m
Far range	436 m	2700 m
Antenna depression angle	30°	35°
Azimuth 3-dB beamwidth	14°	3.2°
Elevation 3-dB beamwidth	16°	15°

The characteristics of the SAR system described above result in theoretical range and azimuth resolutions of 19 and 2.3 cm, respectively, when assuming a linear flight path [19]. The range sampling rate of 40 MHz supports a maximum possible unambiguous range of 436 m.

B. Navigation

The navigation data that are available by default are obtained from the DJI A2 flight control system [20]. It obtains the GPS information from three DJI GPS-Compass Pro Plus receivers situated on top of the drone. These data are internally merged by applying a Kalman filter using data from the two DJI IMU Pro modules. Low-cost INS often suffer from drift over time, causing inaccurate position and attitude estimates. We avoid

this by using a moving baseline. Fig. 1 shows the moving baseline on our drone consisting of four global navigation satellite system (GNSS) AS-ANT2B-HEL-L1L2-SMA-00 helix active antennas [21] mounted on extensions of the drone arms. The geometry of the antennas is formed by a quasi-rectangle pattern of approximately 1 × 2 m. In addition, a Xsens MTi-G-700 INS [22] is placed on top of the drone for data fusion with the moving baseline data.

C. Optical Camera

In addition to the radar, the SAR drone is equipped with a high-end optical camera oriented toward the radar's line of sight, allowing up to 200 frames/s [23]. It has been used until now primarily to validate the radar data.

III. Method

In Section III-A, we demonstrate how to obtain better attitude data using a moving baseline approach. Next, we describe the autofocus method. It corrects for motion errors typically found in SAR data recorded by a drone SAR system.

A. Moving Baseline

The GNSS moving baseline technique is able to provide the attitude without long-term drift, but with a sampling rate of 2 Hz in both L1 and L2 frequencies with noise of about 1° for a baseline larger than 1 m. The quality of the attitude obtained by this technique depends strongly on the external environment and the available visible satellites. In contrast, the attitude obtained by the integration of angular velocities provided by gyroscopes suffers from drift and random walk but is able to provide high-rate data, at several hundred hertz. However, the long-term accuracy of a gyroscope's attitude is low, though the relative accuracy of a gyroscope's attitude can be high (<0.1°) over short durations. In addition, the quality of data provided by the gyroscopes is more consistent and is less influenced by external conditions. In this context, the fusion of both the techniques using a Kalman-filter-based approach should improve the accuracy of the attitude in a large scope and enhance the continuity and the robustness of the attitude determination.

Prior to the experiments, it was ensured that in this configuration, the GNSS signals are not affected by the propellers and the radar. Fixed ambiguities solutions are almost always available when the drone is in a normal flying mode. The Kalman filter solution, at 100 Hz, combining GNSS attitude angles with angular velocities from a three-axis gyroscope, provides an accuracy better than 0.1°.

B. Autofocus

Conventional navigation systems do not achieve the necessary positional accuracy of $\lambda/4 \approx 3$ mm for optimal focusing of the image [24]. Therefore, an autofocus algorithm was developed specifically for nonlinear trajectories using a back-projection processor to correct for these errors. The modified back-projection algorithm used in this article was introduced by Ribalta [25]. As discussed by Frey et al. [17], TDBP offers advantageous performance for nonlinear flight tracks. The approach can be summarized using the following two equations:

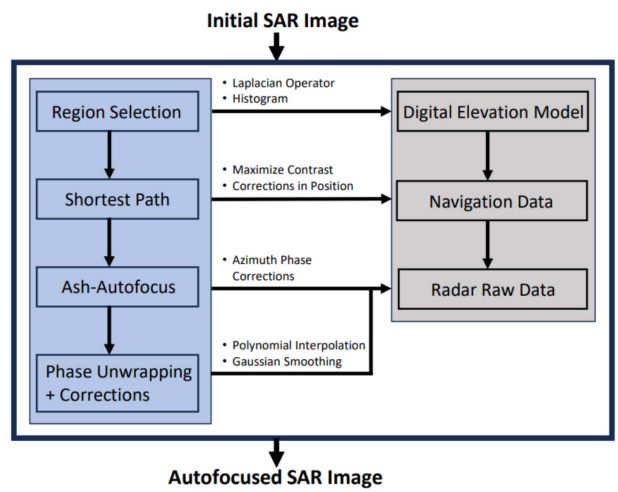

Fig. 2. Flowchart of the proposed autofocus method.

$$s_e(t) = \exp\{-(2\pi j f_0 t + \pi j K t^2)\}, \quad |t| < \frac{T}{2} \tag{1a}$$

$$\tilde{\alpha}(\mathbf{x}) \approx \sum_m \exp\left[\frac{4\pi f_c}{c}(d(\mathbf{x}, \mathbf{p}_{m,0}) - r_c)\right] \times S_m\left(\left(\frac{2K}{c}d(\mathbf{x}, \mathbf{p}_{m,0}) - r_c\right) + \frac{2f_c}{c}v_{\mathbf{x},m}\right). \tag{1b}$$

Equation (1a) describes the formula for the transmitted signal $s_e(t)$ with carrier frequency f_0, chirp rate $K = B/T$, and sweep time T. The backscatter $\tilde{\alpha}$ at position $\mathbf{x}$ of the digital elevation model (DEM) is calculated, as described in (1b). The distance between the sensor position $\mathbf{p}_{m,t}$ at time t during the mth pulse and $\mathbf{x}$ is given by $d(\mathbf{x}, \mathbf{p}_{m,t})$, r_c is the range distance to the center of the imaged region, $f_c = f_0 - 2Kr_c/c$, and $v_{\mathbf{x},m}$ is the derivative of $d(\mathbf{x}, \mathbf{p}_{m,t})$ at $t = 0$. S_m is the Fourier transform of the received signal after demodulation.

Given that for nonlinear flight paths, the shape of the phase correction curve is difficult to predict, we propose a nonparametric autofocus method based on contrast maximization [26]. The algorithm is divided into four main parts, one of which is based on Ash's autofocus method [16]. A flowchart of the algorithm is shown in Fig. 2. The correction steps in the algorithm are described in the blue rectangle on the left. The arrows show the effects of each on the respective raw data in the gray rectangle.

The starting point is the SAR image $\mathbf{M}$ focused with TDBP using the original telemetry data. This image is often smeared in the azimuth direction but can also be subject to errors in the range direction. Since not all the image areas contain useful information for corrections, suitable regions are selected. This is done by convolving the Laplacian $\mathbf{D}$ operator with $\mathbf{M}$

$$M_{\text{Lap}} = M * D, D = \begin{pmatrix} 0 & -1 & 0 \\ -1 & 4 & -1 \\ 0 & -1 & 0 \end{pmatrix} \tag{2}$$

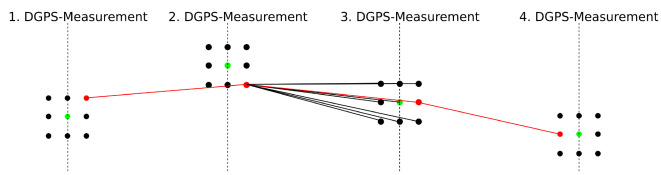

Fig. 3. Shortest path illustration for four position measurements.

where $*$ is the convolution operator. A histogram hist (M_{Lap}) is then used to select the outer 10 percentiles of the pixels. Small areal gaps are closed with a morphological dilation operator. With that information, it is decided which part of the range-compressed data is to be processed at each azimuth time.

In the next step, a shortest path algorithm is applied to correct for large deviations from the true flight trajectory [15]. As the name suggests, it is about optimizing a path with respect to a metric. For optical images, there are numerous studies investigating optimal sharpness metrics [27], [28]. Since optical images share similarities with high-resolution SAR images, it is evident to use their findings for initial focusing steps. The conducted experiments showed that the family of Laplacian-based operators exhibited the best overall performance at normal imaging conditions [28]. For these reasons, after comparing the performance of different metrics over different scenes, the Laplacian variance was used as the metric for the shortest path algorithm.

The principle of the shortest path algorithm is illustrated in Fig. 3. DGNSS measurements (or only GNSS measurements, if only these are available) are used as support points $\mathbf{P_i}, i \in [0, M]$, where M is the number of support points. They are marked as green dots in the illustration. The search starts at the first position measurement and ends at the last one. Homogeneously distributed test points $\mathbf{P_{i,k}}$, with spacing Δs, are then created around the support points

$$\mathbf{P_{i,(k,l,m)}} = \mathbf{P_i} + \Delta s \cdot (k\hat{x} + l\hat{y} + m\hat{z}) \tag{3}$$

with unit vectors $\hat{x}$, $\hat{y}$, and $\hat{z}$ and $k, l, m \in \mathbb{Z}$. They are symbolized using black dots. The spacing Δs between these points is dependent on the initial accuracy of the supporting points (DGNSS or GNSS measurement). It also has to be chosen small enough so that a change in the position by Δs does not cause the projections of pulses to different cells in the map. Subapertures are then processed between the test points of neighboring support points. The connection maximizing the metric of the entire path is chosen.

Once the shortest path algorithm has corrected the largest error contributions, a variation of Ash's method is applied [16]. His main idea was to trace back the optimization of a convex function, later in his article specified as metric $\Psi(x) = x^2$

$$s(\hat{\Phi}) = \sum_i \Psi\left(v_i(\hat{\Phi})\right) = \sum_i \left(v_i(\hat{\Phi})\right)^2 \tag{4a}$$

$$\hat{\Phi} = \arg\max_{\Phi} s(\Phi) \tag{4b}$$

to an ellipsoidal geometry problem. Thereby, $\Phi = (\Phi_i), i \in [1, \ldots, N]$, is the per-pulse phase correction for an aperture formed by N pulses, and $v_i(\hat{\Phi})$ is the intensity of the ith pixel resulting from a particular set of phase error estimates $\hat{\Phi}$. The intensity-squared sharpness was chosen as this metric was shown to be the limiting form solution of the maximum likelihood estimation and the maximum posterior estimation for ideal SAR data [29]. However, as shown by Fienup and Miller [26], the best choice of a metric is scene dependent.

An important modification was added to Ash's method. To guarantee the numerical stability of the calculation, a scaling factor κ is introduced. When switching to the new coordinate system, $\tilde{a}$ and $\tilde{b}$ have to be replaced with $\tilde{a}_\kappa = \tilde{a}/\kappa$ and $\tilde{b}_\kappa = \tilde{b}/\kappa$, respectively. Consequently, the eigenvalues of the following calculations must be scaled back correctly by $\lambda_1 = \lambda_{1,\kappa} \cdot \kappa^2$ and $\lambda_2 = \lambda_{2,\kappa} \cdot \kappa^2$ before calculating the phase correction.

Since the phase corrections obtained by Ash's method are range independent, no frequency shifts can occur in the range-compressed data. This is simply explained by the Fourier shift theorem for the frequency domain

$$\mathcal{F}\{s(t)\exp(jat)\} = \hat{s}(f - a/2\pi). \tag{5}$$

For FMCW range-compressed data, each frequency is directly related to range through $f_r = 2RK/c$. Therefore, using the TDBP, as described in (1b), will result in errors when dealing with large deviations from the true flight path. In order to mitigate such errors, the preliminary correction step in the shortest path algorithm was necessary.

Once the per-pulse phase corrections Φ are calculated using Ash's method, phase unwrapping is applied. Since the phase is directly related to the slant range, it should follow a steady physically reasonable course. Incorrect phase unwrapping results in jump points. These are identified by first smoothing the phase with a Gaussian filter and then examining the slope of the curve. Then, a thresholding step is applied in order to remove the outliers with the following expression:

$$\Phi = \begin{cases} \Phi, & \text{if } \frac{d\Phi}{dt} \leq k \\ \text{remove}, & \text{otherwise} \end{cases} \tag{6}$$

where k depends on the pulse repetition frequency and the dynamics of the system. By means of local polynomial interpolation around the jump points, the corrected phase jump is determined. The previously deleted outliers are finally replaced using interpolated values, and the phase correction of the subaperture is obtained.

The phase corrections of the individual subapertures must be combined in the final step. For this purpose, the ends of the phase corrections are adjusted to each other by subtracting or adding a multiple of 2π. Finally, the combined phase corrections are smoothed with a Gaussian filter. If the raw data are multiplied by the factor $\exp(-j\Phi)$ and then combined with the corrected navigation data from the shortest path algorithm using TDBP, the backscatter map that results is the corrected SAR image.

IV. Results

The capabilities of the radar are demonstrated in the following with data acquired over four different test sites. To measure the

spatial resolution of the focused SAR images, four corner reflectors with identical azimuth orientation, aligned to the planned flight track, were placed on a flat lawn surface. The reflectors were illuminated at a height of 66 m, with a distance of the closest approach of approximately 105 m.

In the second test site, SAR images of urban structures, such as buildings, streets, and moving cars, were acquired from a height of approximately 70 m. The primary objective was to emphasize the enhanced ranging capability of the sensor in an urban setting.

Finally, recordings from the drone were synchronized with the MIRANDA35 airborne sensor at two specific test sites. The day following MIRANDA's airborne flight, we operated the drone under identical sunny weather conditions. Unfortunately, simultaneous flights were not possible due to technical issues. During the first flight, both the platforms were set to have the same heading. In the second scene, different headings were selected.

All the images were focused using TDBP. In a subsequent step, the autofocus method was applied to the drone-based data, as described in Section III-B.

The focusing quality after autofocus was validated based on the signatures of corner reflectors deployed in the test sites. The focusing performance was tested against original Ash's algorithm. For this purpose, favorable initial conditions were used for Ash's algorithm (no major deviations from the ideal flight path).

Validation was conducted by comparing the images acquired by the drone and MIRANDA35 [18]. Table I lists the main parameters of MIRANDA35 and the drone's Radarbook2. Despite differences in carrier frequencies and bandwidths, the resulting focused images were sufficiently similar to enable meaningful comparisons. It is important to note that the MIRANDA35 sensor was mounted on an ultralight aircraft, making it more susceptible to external factors like wind and turbulence in comparison to larger airborne platforms.

A. Experiment 1

The results of experiment 1 are shown in Fig. 4. In Fig. 4(a), the impact of autofocus on the signature of the reflectors is highlighted. Analyzing the signatures of the reflectors in range and in azimuth in Fig. 4(b) and (c), a mean range 3-dB impulse response width (IRW) of $\delta r = 19 \pm 1.1$ cm and an azimuth IRW of $\delta az = 2.5 \pm 0.2$ cm were observed. Each reflector signature is, thereby, normalized individually to its maximum for visualization purposes. Comparing them to the theoretically achievable resolutions of $\delta r = 19$ cm and $\delta az = 2.3$ cm demonstrates that the maximum focusing quality was nearly reached. Regarding the azimuth peak sidelobe ratio (PSLR), an average value of $\text{PSLR}_{\text{az}} = -10.9 \pm 1.3$ dB was obtained. The average integrated sidelobe ratio (ISLR) in azimuth was $\text{ISLR}_{\text{az}} = -6.3 \pm 2.4$ dB. A summary of the individual azimuth values of each reference reflector can be found in Table II. In addition, the values observed after the application of Ash's method are added for comparison in the middle of each column. The range IRW after the application of autofocus was 19.4, 17.9, 17.9, and 20.6 cm for reflectors 1–4, respectively. No comparison is listed for the range IRW, as the autofocus step mainly affects the azimuth dimension.

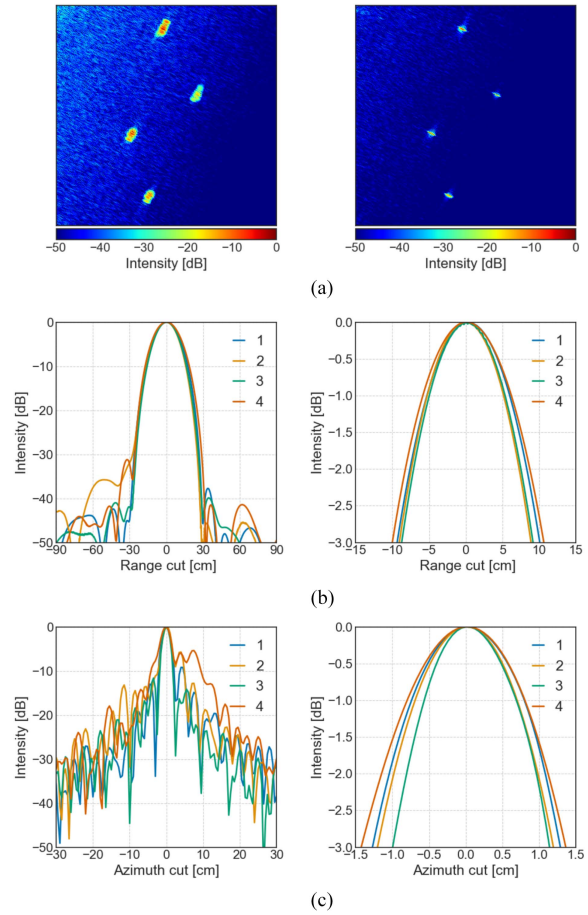

Fig. 4. Range and azimuth resolution derived from four reference reflectors. (a) Reflectors before and after application of autofocus. In (b) and (c), the curves give information about the IRW and the PSLR after autofocus in the range and azimuth dimensions.

TABLE II
AZIMUTH SIGNATURE ANALYSIS OF THE REFLECTORS BEFORE AUTOFOCUS/CORRECTION WITH ASH'S ALGORITHM/CORRECTION WITH THE PROPOSED METHOD

Reflector	IRW [cm]	PSLR [dB]	ISLR [dB]
#1	4.7/2.6/2.6	−2.7/−10.8/−11	4.7/−7.8/−7.9
#2	2.1/2.1/2.1	−1/−13.1/−10.1	5.1/−8.9/−8.9
#3	2.5/2.4/2.4	−1/−8.5/−9.6	8.3/−4.7/−5.7
#4	2.7/2.8/2.8	−0.8/−9.9/−10.9	9.7/−2.6/−2.6

For the calculations above, a broadening factor of 1.62 from the application of a Hanning filter in range was corrected, while the sidelobes were still suppressed [19]. No filtering was applied in the azimuth direction.

B. Experiment 2

For this analysis, we did not utilize the measured lever arms and processed once with the attitude data of drone navigation

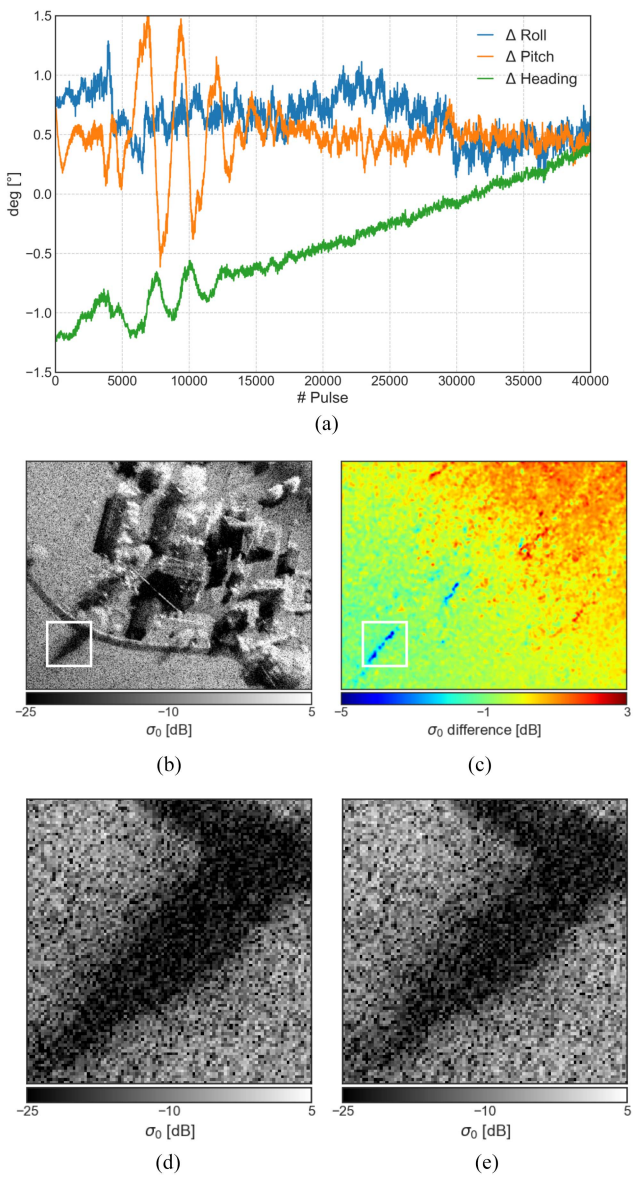

Fig. 5. Improvements from the moving baseline method. Subtracting the attitude values provided by the moving baseline data from those observed from the drone's internal data resulted in the plots shown in (a). (b) SAR image processed with moving baseline attitude data. Subtracting the image with internal data results in (c). (d) Highlighted area in (b) for the moving baseline and (e) for the internal attitude data.

data and once with the estimates from the moving baseline system. The improvement achieved by the moving baseline method is shown in Fig. 5. Fig. 5(a) shows the difference between the moving baseline and the drone's internal attitude retrieval versus the A2 flight control system for a single acquisition. It is noticeable that there is a constant drift in the heading. While the moving baseline heading is nearly constant, the internally measured heading changes. Fig. 5(b) illustrates the sigma naught σ_0 backscatter [30] processed with the moving baseline data. Subtracting from it the image obtained with the DJI attitude data and smoothing it slightly with a Gaussian filter, one obtains Fig. 5(c). The area indicated with the white rectangle is shown in Fig. 5(d) for the moving baseline and in Fig. 5(e) for the internal DJI attitude data. A dynamic range of 116.1 dB was observed for the area shown in Fig. 5(b) for the moving baseline method and 115 dB without it. Extracting the noise-equivalent sigma zero (NESZ) from the shadow in the highlighted scene, −23.7 dB was found for Fig. 5(d) and −22.4 dB for Fig. 5(e).

C. Experiment 3

Focusing the SAR image of the third experiment by applying the proposed autofocusing technique leads to the result shown in Fig. 6(a). The near range edge, running diagonally in the upper left of the image, is at a range of approximately 84 m from the drone. In Fig. 6(b), an enlarged area of the SAR image from Fig. 6(a) is compared to an optical airphoto reference image from swisstopo [31].

The improvement in image quality achieved with the autofocus algorithm is highlighted in Fig. 7 for two scenes. In Fig. 7(a), a building with a complex facade is shown *before* the correction with autofocus. The image corrected by using Ash's method is shown in Fig. 7(c). The result *after* application of the proposed method is shown in Fig. 7(e). In the second selected area in Fig. 7(b), the signature of the placed reflector is highlighted by a yellow square. An azimuth IRW of $\delta az = 2.3$ cm, a PSLR of −14.3 dB, and an ISLR of −10.6 dB were observed after autofocus, nearly reaching the theoretical resolution. Before the correction, the IRW was 2.8 cm, the PSLR was −1 dB, and the ISLR was 11 dB. Furthermore, dividing the total summed intensity after applying the correction, by the one before autofocus, gives a factor of 1.086 for scene (a) and 0.975 for (b). Using Ash's method, an IRW of $\delta az = 2.4$ cm, a PSLR of −11.5 dB, and an ISLR of −5.1 dB were observed. Dividing the total summed intensity after applying Ash's method, by the total summed intensity before the corrections, gives ratios of 0.979 and 0.984 by way of comparison. The ratio calculated by dividing the total summed intensity after applying the correction from the proposed method and the one after Ash's method gives 1.109 and 0.99. In terms of entropy, Ash's method led to an increase by factors of 1.094 and 1.068. The proposed method was able to reduce it by factors of 0.993 and 0.994. For the scene in the left column, a dynamic range of 111.4 dB was observed before autofocus, 110.3 dB with Ash's method, and 117.3 dB after our method. In the same order, the NESZ in Fig. 7(a), (c), and (e) was −22.5, −18.6, and −22.3 dB, respectively. The scene in the right column gave a dynamic range of 112.6, 120.8, and 113 dB for Fig. 7(b), (d), and (f) with an NESZ of −33.6, −19.2, and −33 dB, respectively.

D. Experiment 4

Comparison between the Radarbook2 and MIRANDA35 is given in Fig. 8. The reflector analysis in the SAR image of the Radarbook2 is listed in Table III under Exp 4A. The dynamic range before autofocus was 114.8 dB, 117.3 dB with Ash's method, and 123.8 dB with the proposed algorithm. In the same order, an NESZ of −25.6, −17, and −25.6 dB was achieved. The analysis of the flight data shows that the antenna headings of both the sensors were similar, deviating from each other by a maximum of 5° over the course of their acquisitions.

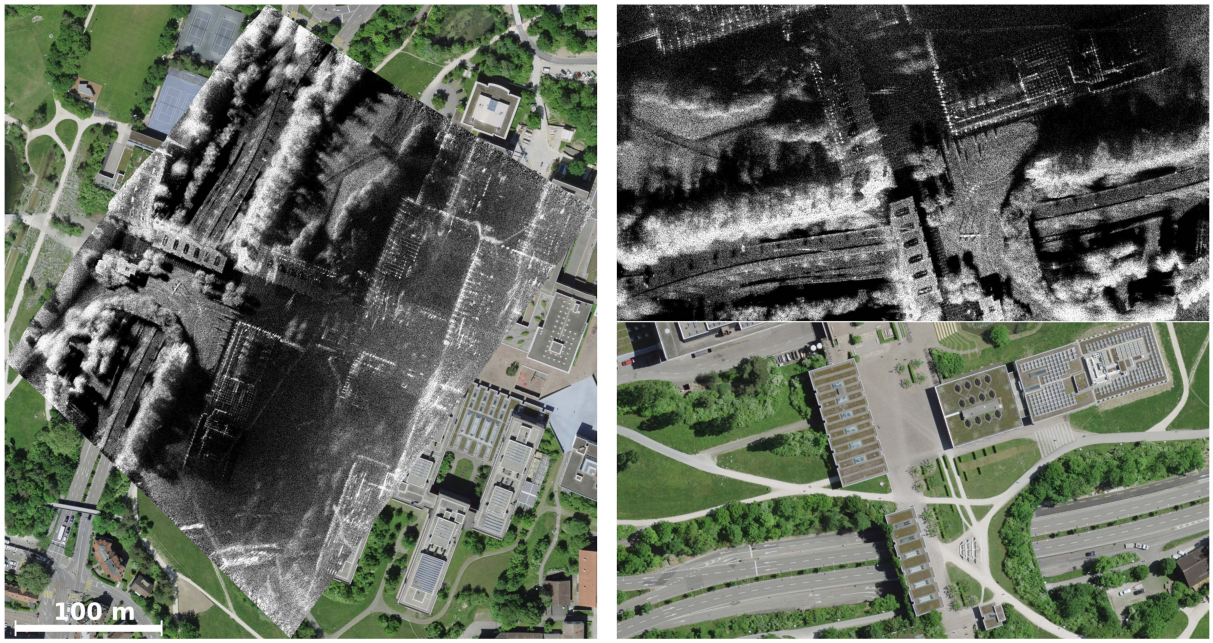

(a) (b)

Fig. 6. Drone-based SAR acquisition of urban area. (a) Image processed for a large swath. (b) Comparison with an RGB optical image from swisstopo [31].

TABLE III
AZIMUTH SIGNATURE ANALYSIS OF THE REFLECTORS BEFORE AUTOFOCUS/CORRECTION WITH ASH'S ALGORITHM/CORRECTION WITH THE PROPOSED METHOD

Reflector	IRW [cm]	PSLR [dB]	ISLR [dB]
Exp 3	2.8/2.4/ 2.3	−1/−11.5/−11	11/−5.1/−10.6
Exp 4A	5/3.5/ 3.4	−5.1/−16.5/−16.5	5.1/−11/−10.9
Exp 4B #1	2.9/2.6/ 2.6	−0.9/−16/−15.6	9.5/−12.3/−11.7
Exp 4B #2	4.2/3.6/ 2.7	−1.2/−3.4/−16.6	6/−10.9/−12.7

The second comparison is presented in Fig. 9. In addition to the images from the Radarbook2 in Fig. 9(a) and MIRANDA35 in Fig. 9(b), an optical image from Swisstopo is shown in Fig. 9(c). In contrast to the first comparison, the sensors, here, had different headings (35° on average) during the flight. The azimuth signature analysis of the two reflectors in the SAR image from the Radarbook2 is listed in Table III under Exp 4B #1 and #2. The dynamic range before autofocus was 146.8 dB, 149.4 dB with Ash's method, and 155.6 dB with the proposed algorithm. In the same order, an NESZ of −21.3, −12.8, and −21.5 dB was achieved.

In Fig. 10, we show an SAR image with the radar shadows caused by two moving cars, highlighted by the two yellow arrows. The image was focused using 200 pulses. The backscatter of car 2 is indicated by a yellow rectangle. The existence of the cars was verified using optical images from the onboard camera.

V. DISCUSSION

A. Experiment 1

The experiment with the four reflectors showed that the theoretically possible range IRW was achieved. Smaller values than 19 cm were achieved with reflectors 2 and 3. This could be explained by the fact that the bandwidth is possibly slightly larger than specified. Interpolation errors that could occur while determining the 3-dB IRW could also have caused this discrepancy. With the measured azimuth IRW, one is close to the theoretically possible resolution with all the reflectors validating the accuracy of the drone navigation system and the focusing algorithm. Only reflector 4 achieved a slightly worse resolution, as one might expect. This can again be attributed to interpolation errors. The $\mathrm{PSLR_{az}} = -10.9 \pm 1.3$ dB was not as large as one might expect. In the SAR literature, values around −20 dB are typically considered good. However, one must take into account that the reflectors were placed on a lawn, which can have a negative effect on the PSLR. The same argument can be made for the ISLR. Furthermore, it can be observed that for the simple scenario with only reflectors, Ash's algorithm had a similar performance to the newly proposed method.

B. Experiment 2

Assuming that the position is perfectly known, the attitude affects mainly the radiometry and not the focusing quality. The NESZ is generally more suitable to show the improvement offered by using the moving baseline approach than investigating corner reflectors.

As can be observed in Fig. 5(b)–(e), the backscatter maps retrieved using the more accurate moving baseline system had radar shadows that appeared darker than in the other cases. This observation can be supported by the 1.3-dB lower NESZ. Overall, the dynamic range in the image was widened by 1.1 dB by lowering the minimum and increasing the maximum backscatter retrieved.

As can be observed in Fig. 5(c), there was a trend in backscatter from the upper right corner of the image to the lower left corner. This could be explained by the different reference roll

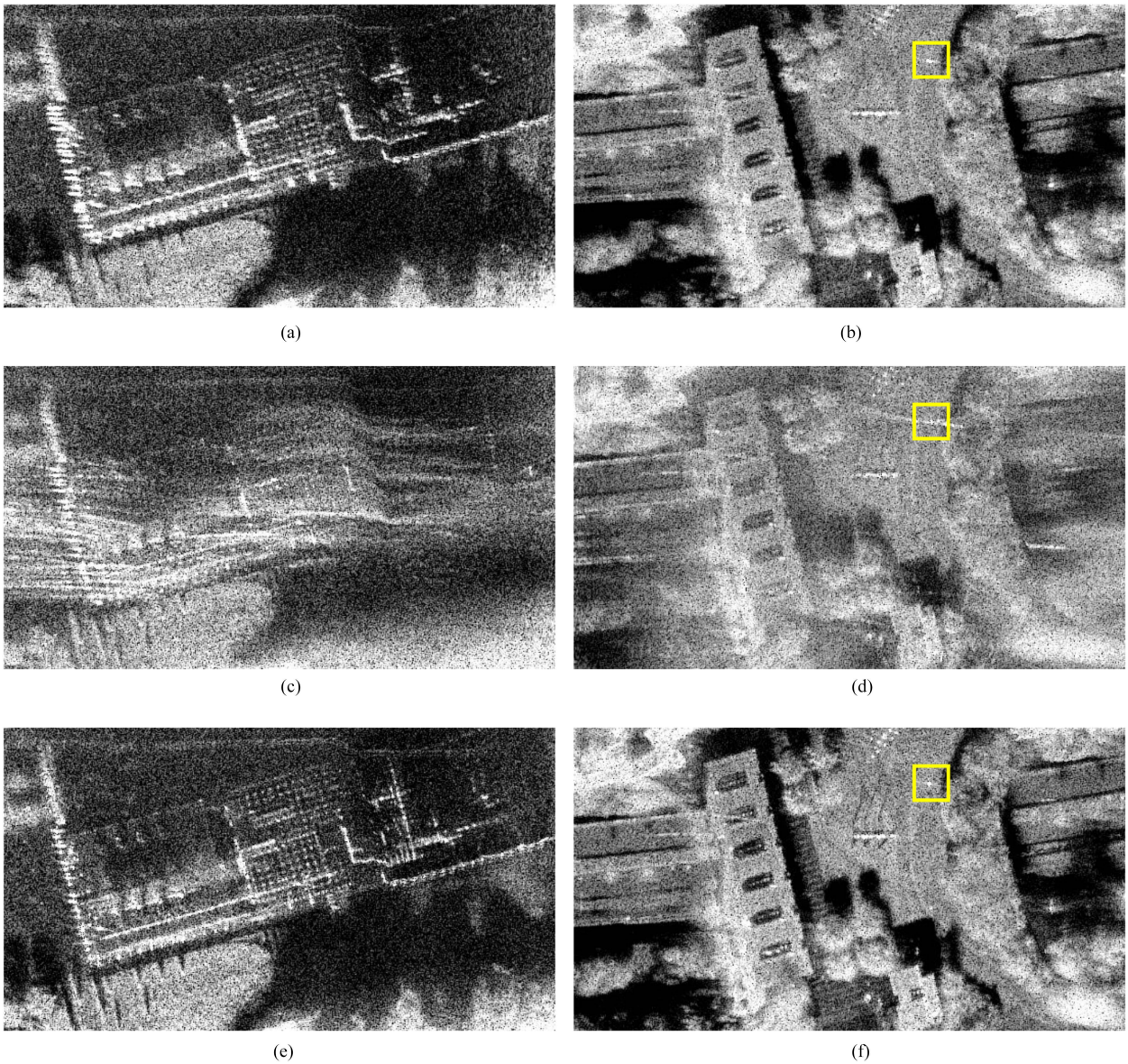

Fig. 7. Effect of the autofocusing algorithm highlighted by two scenes. The first row contains the images before applying corrections. In (a), a building with solar collectors on the roof is shown, which lead to many backscatter points. The scene in (b) showcases the building's forecourt with the reference reflector's signature indicated within the yellow square. The images corrected by using Ash's autofocus method are shown in (c) and (d). The results of the proposed method are given in the last row in (e) and (f).

angles used during backscatter retrieval. As one can see in Fig. 5(a), there is a difference of about 0.5° leading to this effect.

C. Experiment 3

A more detailed overview of the performance capabilities of the system can be seen in Fig. 6. As the flight was planned in such a way that the area around the road was in the main beam of the antenna, this area had the highest contrast. The decrease in contrast outside the main lobe is visible, especially with increasing far range extending well above the 16° elevation angle of the antenna. Nevertheless, the contours of the buildings are clearly recognizable. Radiometric corrections using the antenna diagram were applied to compensate for the backscatter differences. However, not all the contrast issues could be compensated, since it is given by the physical magnitude of the radiated power. Looking at the buildings in the distance, it is noticeable that there is sometimes a bright signature similar to a signature veil over them. Since the azimuth IRW measured at the reflector was actually close to the theoretical achievable value, this cannot be attributed to poor focusing. Even by looking at the optical images acquired by the onboard camera, it is not clear where these artifacts originated. One possible explanation could be multipath reflections from the complex roof structures of the buildings.

The detailed view of the autofocus effect on the SAR images in Fig. 7 shows the scope of the improvements. The azimuth signature values of the reflector are listed in Table III. In Fig. 7(a), the typical case of rectangular buildings is shown. The energy of the scatterers is focused by maximizing the intensity during

(a) (b)

Fig. 8. Validation of the drone image in (a) against the image from the MIRANDA35 sensor in (b) while having the same heading during acquisition.

(a) (b) (c)

Fig. 9. Validation of the drone image in (a) against the image from the MIRANDA35 sensor in (b) and an optical image from swisstopo in (c) [31].

autofocus. This results in emphasizing the edges of the buildings. However, looking at the summed intensity ratio of 1.086 and 0.975 shows that maximizing the energy over entire scene is not preferable. While maximizing total intensity works for urban scenes as in Fig. 7(a) without much vegetation, it cannot be a reliable metric for scenes with more vegetation, as seen in Fig. 7(b). This highlights why only selected regions should be used for improving the focusing.

The widening of the measured image dynamic range after applying the autofocus method was clearly shown in Fig. 7. It was improved by 5.9 dB in Fig. 7(e) and 0.4 dB in Fig. 7(f). Surprisingly, the NESZ increased slightly after the autofocus corrections by 0.2 dB in Fig. 7(e) and 0.6 dB in Fig. 7(f). This could be attributed to the shadow of the trees not being an ideal nonreflective area. Radiation could partially penetrate through gaps and contribute to the backscatter of shadowed areas. Another possible explanation might be compression gain due to the use of better navigation data.

Differences between the backscatter maps retrieved via the proposed method compared to using Ash's algorithm are

Fig. 10. Two cars driving on the road. Their radar shadow is highlighted in the SAR image by two arrows. On the right is the corresponding image from the onboard camera.

obvious from a visual point of view. The worse NESZ highlights a problem with Ash's method. It is 3.7 dB higher for Fig. 7(c) and 13.8 dB higher for Fig. 7(d). This reflects itself also in the worse ISLR of the reflector. Interestingly, while having a worse dynamic range in Fig. 7(c), Ash's method has a 7.8 dB higher one in Fig. 7(d). This could originate from it optimizing the reflected intensity of natural targets like trees leading to degenerated performance over the entire scene.

Estimation of residual motion errors can also be performed by processing a set of SAR images with different squint angles, also called squints [32], [33]. Ideally, the phase difference between the squint images corresponds to the difference of the residual motion error, i.e., to the local derivative of the error. Integrating it leads to the residual error itself. However, this approach works only for point-like targets and not for distributed targets. The interferometric phase derived with two consecutive squints of the SAR image did not show range- or azimuth-dependent phase screens. Similar results were obtained when using four consecutive squints.

Toward far range, it looks like there might be a degradation in the focusing quality of the buildings. Since we did not place corner reflectors from near to far range, it is difficult to verify such tendencies. Analysis of the scatterers of buildings at different ranges and the multisquint analysis above could not verify such a trend. Nonetheless, this phenomenon was also observed in images acquired by other FMCW drone SAR systems [34], [35]. Considering that these systems operate at lower frequencies (L-, S-, and X-bands), they are expected to be more robust to motion errors. Therefore, one might speculate that these errors were introduced by the FMCW hardware system itself rather than by inaccuracies in the navigation data.

D. Experiment 4

The comparison with the image of the MIRANDA35 sensor in Fig. 8 shows a great degree of similarity. The differences are in the details. Given that the MIRANDA35 platform has a well-calibrated elevation antenna pattern that is corrected during processing, and that it flies much higher and, thus, has a much wider swath width, the backscatter values in the image are "flatter," i.e., more evenly distributed. In addition, the 5° difference in depression angle caused longer radar shadows in the images from Radarbook2. As the acquisitions did not take place at exactly the same time, some of the farm's cars and agricultural machinery were placed differently. This was verified by both platforms' optical onboard cameras, as shown in the example highlighted by the yellow square in Fig. 8.

The differences between the headings of the two sensors make it more difficult to draw conclusions from the comparison in Fig. 9. Different scatterers within each objects were sometimes active. Thus, one can see that the lower left house in the MIRANDA35 sensor is oversaturated due to an unfavorable radiation angle. The Radarbook2 showed more details of the same building. Nevertheless, a great deal of agreement can be observed here as well. As a brief analysis has shown, it is even possible to extract the speed and position of cars from the SAR images. There were many other cars in and around the roundabout whose signatures appeared smeared due to their individual Doppler histories. The smeared signatures in the drone images look stronger than in the one of MIRANDA35 due to the different traffic state during the acquisitions.

Comparing the performance against Ash's algorithm through the azimuth signature analysis, Table III shows only minor differences for most of the reflectors, with Exp 4B #2 being the exception. The better result for Exp 4B #2 can be explained by the larger number of natural targets in the form of trees entering the image around this azimuth time. Looking at the global properties, the dynamic range and the NESZ were significantly better for the proposed algorithm than for Ash's method over both the scenes. In addition, it is possible that moving objects had a negative impact on the performance of the algorithm. They can be filtered out when selecting the region (see Fig. 2). For this purpose, one can use: 1) along track interferometry with multiple channels; 2) subaperture or multisquint approaches [36]; and 3) the use of virtual channels [37].

E. Autofocus

The proposed autofocus method proved itself across a variety of scenarios. Both the SAR images showing very urban and partially rural regions were focused with high quality. Obviously, the performance of the algorithm improved as the number of strong scatterers in the image increased. However, this was true for all the autofocus methods. Since the algorithm was designed for a simple stripmap mode, there may not be any prominent scatterers in the beam at certain azimuth times. Testing such scenarios has shown that, in this case, the last step of optimization using Ash's method does not bring any additional improvements. Consequently, the optimal path method, optimizing the Laplace variance, is especially important for the pulses during this azimuth time.

As mentioned in the discussion in Section V-D, the quality of the algorithm deteriorates if there are several moving objects in the image. In this case, one has to filter them out first. Another limitation arises from the overlay effects of very tall buildings. If they are projected onto a digital terrain model with TDBP, they are naturally more defocused in the direction of the roof. Because of this defocusing effect, one should not attempt to correct motion errors with information from tall buildings. Focusing these targets with a digital surface model can solve this problem.

VI. Summary and Outlook

In this article, we presented a SAR drone system operating at K-band with improved adjustable transmission power. Possessing a transmit power of up to 50.8-dBm EIRP, imaging of objects at a distance of up to 400 m was possible. Furthermore, an image-sharpness-based autofocus algorithm was presented to correct for orientation-jitter-induced phase errors. The combination of the shortest path algorithm together with Ash's refinement step was able to correct even larger errors. The fact that it can be used in a back-projection framework with a DEM is advantageous, since improvements of the computation power of GPUs have reduced the importance of frequency-based focusing.

An experiment with four corner reflectors showed that a near-optimal range and azimuth resolution of $\delta r = 19$ cm and $\delta az = 2.5$ cm, respectively, could be achieved. Furthermore, the impact of the moving baseline and the autofocus method was demonstrated. Additional insights into the performance of the drone system were gained through comparisons with the airborne MIRANDA35 sensor. Comparisons with a high-resolution airborne system showed that the hardware and software developed in this project is a further important step toward drone-based SAR systems that are flexible, cost efficient and are capable of producing high-quality products.

In the future, more detailed radiometric analysis leading to an enhanced radiometric calibration and advanced experiments will be performed. As shown in Fig. 10, the drone SAR system is sensitive enough to detect and image moving vehicles on the ground. Hence, further research tracking ground moving targets and tomographic examinations are envisaged. For this purpose, it is planned that the multibaseline capabilities of the sensor, which were not used in these experiments, will be exploited. Owing to the structure of the algorithm, many steps can be parallelized. An implementation taking advantage of this property is envisioned. However, since the TDBP benefits greatly from a high-power GPU, onboard processing would be unfavorable. To consider such a solution, a fast factorized back projection might be needed instead of TDBP.

Acknowledgment

The authors would like to thank all the people and the institutions involved during the MIRANDA35 and the drone experiments.

References

[1] M. Lort, A. Aguasca, C. López-Martínez, and T. M. Marín, "Initial evaluation of SAR capabilities in UAV multicopter platforms," *IEEE J. Sel. Topics Appl. Earth Observ. Remote Sens.*, vol. 11, no. 1, pp. 127–140, Jan. 2018.

[2] M. G. Fernández et al., "Synthetic aperture radar imaging system for landmine detection using a ground penetrating radar on board a unmanned aerial vehicle," *IEEE Access*, vol. 6, pp. 45100–45112, 2018.

[3] E. Schreiber, A. Heinzel, M. Peichl, M. Engel, and W. Wiesbeck, "Advanced buried object detection by multichannel, UAV/drone carried synthetic aperture radar," in *Proc. 13th Eur. Conf. Antennas Propag.*, 2019, pp. 1–5.

[4] M. Schartel, R. Burr, W. Mayer, N. Docci, and C. Waldschmidt, "UAV-based ground penetrating synthetic aperture radar," in *Proc. IEEE MTT-S Int. Conf. Microw. Intell. Mobility*, 2018, pp. 1–4.

[5] D. Luebeck et al., "Drone-borne differential SAR interferometry," *Remote Sens.*, vol. 12, no. 5, 2020, Art. no. 778.

[6] L. Moreira et al., "A drone-borne multiband DInSAR: Results and applications," in *Proc. IEEE Radar Conf.*, 2019, pp. 1–6.

[7] O. Frey, C. L. Werner, and R. Coscione, "Car-borne and UAV-borne mobile mapping of surface displacements with a compact repeat-pass interferometric SAR system at L-band," in *Proc. IEEE Int. Geosci. Remote Sens. Symp.*, 2019, pp. 274–277.

[8] G. Oré et al., "Predicting sugarcane harvest date and productivity with a drone-borne tri-band SAR," *Remote Sens.*, vol. 14, no. 7, 2022, Art. no. 1734.

[9] A. Bekar, M. Antoniou, and C. J. Baker, "Low-cost, high-resolution, drone-borne SAR imaging," *IEEE Trans. Geosci. Remote Sens.*, vol. 60, 2022, Art. no. 5208811.

[10] W. Liu, H. Feng, and Y. Lu, "Ka-band drone SAR flying without GPS," in *Proc. 7th Asia-Pacific Conf. Synthetic Aperture Radar*, 2021, pp. 1–4.

[11] Y. Luomei, F. Xu, F. Wang, and Y. Dong, "Demonstration of simultaneous localization and imaging with multirotor-borne MiniSAR," *IEEE J. Sel. Topics Appl. Earth Observ. Remote Sens.*, vol. 15, pp. 6548–6558, 2022.

[12] J. Svedin, A. Bernland, A. Gustafsson, E. Claar, and J. Luong, "Small UAV-based SAR system using low-cost radar, position, and attitude sensors with onboard imaging capability," *Int. J. Microw. Wireless Technol.*, vol. 13, no. 6, pp. 602–613, 2021.

[13] INRAS, "Radarbook2," 2022. Accessed: Jan. 15, 2022. [Online]. Available: https://inras.at/en/radarbook2/

[14] E. W. Dijkstra, "A note on two problems in connexion with graphs," *Numer. Math.*, vol. 1, pp. 269–271, 1959.

[15] P. E. Hart, N. J. Nilsson, and B. Raphael, "A formal basis for the heuristic determination of minimum cost paths," *IEEE Trans. Syst. Sci. Cybern.*, vol. SSC-4, no. 2, pp. 100–107, Jul. 1968.

[16] J. N. Ash, "An autofocus method for backprojection imagery in synthetic aperture radar," *IEEE Geosci. Remote Sens. Lett.*, vol. 9, no. 1, pp. 104–108, Jan. 2012.

[17] O. Frey, C. Magnard, M. Ruegg, and E. Meier, "Focusing of airborne synthetic aperture radar data from highly nonlinear flight tracks," *IEEE Trans. Geosci. Remote Sens.*, vol. 47, no. 6, pp. 1844–1858, Jun. 2009.

[18] S. Stanko et al., "SAR with MIRANDA-millimeterwave radar using analog and new digital approach," in *Proc. Eur. Radar Conf.*, 2011, pp. 214–217.

[19] I. G. Cumming and F. H. Wong, "Digital processing of synthetic aperture radar data," *Artech house*, vol. 1, no. 3, pp. 108–110, 2005.

[20] DJI, "A2 impossible precise—A new standard in flight control," 2023. Accessed: Jul. 14, 2023. [Online]. Available: https://www-v1.dji.com/a2.html/

[21] Ardusimple, "Lightweight helical antenna for multiband GNSS (IP67)," 2023. Accessed: Jul. 14, 2023. [Online]. Available: https://www.ardusimple.com/product/helical-antenna/

[22] *MTi User Manual*, Xsens, Enschede, The Netherlands, 2020. Accessed: Jul. 15, 2023. [Online]. Available: https://xsens.com/hubfs/Downloads/usermanual/MTi_usermanual.pdf

[23] *DFK 33UX174—USB 3.0 Color Ind. Camera*, Imaging Source Europe GmbH, Bremen, Germany, 2019. Accessed: Feb. 14, 2020. [Online]. Available: https://www.theimagingsource.com/products/industrial-cameras/usb-3.0-color/dfk33ux174/

[24] W. G. Carrara, R. S. Goodman, and R. M. Majewski, *Spotlight Synthetic Aperture Radar: Signal Processing Algorithms*. Norwood, MA, USA: Artech House, 1995.

[25] A. Ribalta, "Time-domain reconstruction algorithms for FMCW-SAR," *IEEE Geosci. Remote Sens. Lett.*, vol. 8, no. 3, pp. 396–400, May 2011.

[26] J. R. Fienup and J. J. Miller, "Aberration correction by maximizing generalized sharpness metrics," *J. Opt. Soc. Amer. A*, vol. 20, no. 4, pp. 609–620, Apr. 2003.

[27] H. Mir, P. Xu, and P. van Beek, "An extensive empirical evaluation of focus measures for digital photography," *Proc. SPIE*, vol. 9023, 2014, Art. no. 90230I.

[28] S. Pertuz, D. Puig, and M. A. Garcia, "Analysis of focus measure operators for shape-from-focus," *Pattern Recognit.*, vol. 46, no. 5, pp. 1415–1432, 2013.

[29] T. J. Schulz, "Optimal sharpness function for SAR autofocus," *IEEE Signal Process. Lett.*, vol. 14, no. 1, pp. 27–30, Jan. 2007.

[30] D. Small, "Flattening gamma: Radiometric terrain correction for SAR imagery," *IEEE Trans. Geosci. Remote Sens.*, vol. 49, no. 8, pp. 3081–3093, Aug. 2011.

[31] Swisstopo, "SWISSIMAGE—The digital color orthophotomosaic of switzerland," 2022. Accessed: Dec. 27, 2022. [Online]. Available: https://swisstopo.admin.ch/en/geodata/images/ortho.html

[32] P. Prats and J. J. Mallorqui, "Estimation of azimuth phase undulations with multisquint processing in airborne interferometric SAR images," *IEEE Trans. Geosci. Remote Sens.*, vol. 41, no. 6, pp. 1530–1533, Jun. 2003.
[33] A. Reigber, P. Prats, and J. Mallorqui, "Refined estimation of time-varyingbaseline errors in airborne SAR interferometry," *IEEE Geosci. Remote Sens. Lett.*, vol. 3, no. 1, pp. 145–149, Jan. 2006.
[34] S.Y. Jeon et al., "UAV-borne bistatic SAR and InSAR experiments in support of STV and SDC target observables," in *Proc. IEEE Int. Geosci. Remote Sens. Symp.*, 2023, pp. 1906–1909.
[35] F. Brigui, S. Angelliaume, N. Castet, X. Dupuis, and P. Martineau, "SAR-light first SAR images from the New Onera SAR sensor on UAV platform," in *Proc. IEEE Int. Geosci. Remote Sens. Symp.*, 2022, pp. 7721–7724.
[36] D. Henke, E. Mendez Dominguez, D. Small, M. E. Schaepman, and E. Meier, "Moving target tracking in single- and multichannel SAR," *IEEE Trans. Geosci. Remote Sens.*, vol. 53, no. 6, pp. 3146–3159, Jun. 2015.
[37] A. Bacci, M. Martorella, D. A. Gray, S. Gelli, and F. Berizzi, "Virtual multichannel SAR for ground moving target imaging," *IET Radar, Sonar Navigat.*, vol. 10, no. 1, pp. 50–62, 2016.

Peter Brotzer (Member, IEEE) was born in Olten, Switzerland, on November 30, 1992. He received the bachelor's and master's degrees in physics from the ETH Zürich, Zürich, Switzerland, in 2016 and 2018, respectively. He is currently working toward the Ph.D. degree with the University of Zürich, Zürich.

His research interests include autofocusing techniques for synthetic aperture radar (SAR) images with an emphasis on drone SAR.

Daniel Henke received the Dipl.-Inf. degree in computer science from Albert-Ludwigs University, Freiburg, Germany, in 2007, and the Ph.D. degree from the University of Zürich, Zürich, Switzerland, in 2014.

His Ph.D. dissertation focused on the development of methods to track objects in remotely sensed data. From 2014 to 2017, he completed his postdoctoral research under a university research grant with the SARLab, University of Zürich, and under the SNF PostDoc mobility grant with the Department of Earth System Science, School of Physics, University of California, Irvine, CA, USA, and the Smithsonian Tropical Research Institute, Panama, Panama. From 2017 to 2022, he was with the Computational SAR Group, SARLab, Remote Sensing Laboratories, University of Zürich. His research interests include synthetic aperture radar processing, moving target indication and change detection techniques, data fusion, signal processing, probabilistic modeling, and earth system science applications using remote sensing data.

David Small (Senior Member, IEEE) received the B.A.Sc. degree in systems design engineering from the University of Waterloo, Waterloo, ON, Canada, in 1988, the M.A.Sc. degree in electrical engineering from the University of British Columbia, Vancouver, BC, Canada, in 1991, and the Ph.D. degree from the Remote Sensing Laboratories, Department of Geography, University of Zürich, Zürich, Switzerland, in 1998.

His Ph.D. dissertation focused on the development of a processing chain for generating digital elevation models from repeat-pass ERS-1/2 data. Since 2013, he has been leading the Environmental SAR Group, SARLab, Remote Sensing Laboratories, University of Zürich. In addition to geometric and radiometric calibration of synthetic aperture radar (SAR) imagery, he works on standardized approaches for terrain flattening to enable analysis ready data products. These are being demonstrated for a wide variety of applications, from SAR-based wet snow mapping in mountainous terrain, to applications in forestry and wide-area cryosphere mapping.

Emiliano Casalini was born in Carrara, Italy, in December 1988. He received the bachelor's and master's degrees (cum laude) in telecommunications engineering from the University of Pisa, Pisa, Italy, in 2011 and 2014, respectively, and the Ph.D. degree from the University of Zürich, Zürich, Switzerland, in 2021.

His Ph.D. dissertation focused on the imaging of moving targets in synthetic aperture radar (SAR) images. He is currently a Postdoctoral Researcher with the University of Zürich. His research interests include indicating and imaging ground moving targets in synthetic aperture radar images, SAR focusing, inverse SAR, interferometry, and other SAR-related techniques.

Sébastien Guillaume received the Dipl.Ing. degree in geomatics and the Ph.D. degree from ETH Zürich, Zürich, Switzerland, in 2007 and 2015, respectively.

His Ph.D. dissertation focused on the determination of the gravity field for the alignment of particle accelerators with CERN, Geneva, Switzerland. He is currently an Associate Professor of Geodesy and Navigation with HEIG-VD, Yverdon-les-Bains, Switzerland. His research interests include geodesy, positioning, navigation, global navigation satellite systems, and virtual reality.

Rolf Vogt received the M.S. and Ph.D. degrees in electrical engineering from ETH Zürich, Zürich, Switzerland, in 1988 and 1996, respectively.

In 1988, he joined Alcatel Switzerland, Zürich, working as an R&D Engineer in the development of microwave radio links. From 1996 to 2005, he was a Project Manager with ETH Zürich. His activities included the design of monolithic integrated circuits for microsensor and wireless telecommunication applications. Since 2005, he has been a Professor of Wireless Communications with the Bern University of Applied Sciences, Biel, Switzerland. His research interests include the design of wireless communication systems and the investigation of radio wave propagation.

Elías Méndez Domínguez (Member, IEEE) received the M.Sc. degree in telecommunications engineering from the University of Vigo, Vigo, Spain, in 2007, and the Ph.D. degree from the University of Zürich, Zürich, Switzerland, in 2018.

His Ph.D. dissertation focused on change detection in urban areas with synthetic aperture radar (SAR) imagery. In 2008, he joined the traineeship program with the Sensors and Radar Technologies and Cybersecurity Unit, Institute for the Protection and Security of the Citizen (Joint Research Centre), Ispra, Italy. In 2009, he joined the Surface Radar Unit, Thales Nederland B.V., Delft, The Netherlands, under the FP7 Marie Curie Early Stage Research Training Program in collaboration with the International Research Centre for Telecommunications and Radar of the Delft University of Technology, Delft. In 2010, he joined the Remote Sensing Laboratories, Department of Geography, University of Zürich, where he has been with the Computational SAR Group, SARLab since 2023. His research interests include advanced pulse compression techniques, radar waveform diversity, and SAR signal and image processing.